Mathematical Models and Algorithms for Processing Retinal OCTA Images

Martina Longaroni[5], Lucrezia Rinelli[1,2], Arianna Travaglini[3,4(✉)], and Gianluca Vinti[1,4]

[1] Department of Mathematics and Computer Science, University of Perugia, 1, via Vanvitelli, 06123 Perugia, Italy
{lucrezia.rinelli,gianluca.vinti}@unipg.it
[2] Department of Mathematics and Computer Science "U.Dini" - DIMAI, University of Florence, 67/a, Viale Giovanni Battista Morgagni, 50134 Firenze, Italy
[3] Department of Engineering, University of Basilicata, 10, V.le dell'Ateneo Lucano, 85100 Potenza, Italy
arianna.travaglini@unibas.it
[4] Department of Mathematics and Informatics, Lucian Blaga University of Sibiu, 5-7, Street Dr. I. Ratiu, 550012 Sibiu, Romania
[5] Fondazione Policlinico Universitario Agostino Gemelli IRCCS, 00168 Rome, Italy
martina.longaroni@policlinicogemelli.it

Abstract. This study investigates the advanced reconstruction capabilities of sampling Kantorovich (SK) operators, emphasizing their remarkable approximation properties and their application to Optical Coherence Tomography Angiography (OCTA) images from both healthy and diabetic patients. By exploiting these mathematical tools, significant enhancements in image reconstruction quality are achieved. Initially, retinal vascular network connectivity is evaluated using an algorithm that computes connected components, comparing non-reconstructed and SK-reconstructed images to demonstrate the advantages of SK-reconstruction. Moreover, SK-reconstructed superficial capillary plexus (SCP) images are analyzed to investigate the foveal avascular zone (FAZ) in both patient groups. The SK algorithm successfully identifies critical morphological differences in the FAZ between healthy and diabetic patients, highlighting the efficacy of SK operators in improving image reconstruction for diagnostic applications.

Keywords: Sampling Kantorovich operators · approximation results · image processing · Optical Coherence Tomography Angiography · cluster counting · FAZ analysis

1 Introduction

The present paper highlights the reconstruction properties of sampling Kantorovich (SK) operators, which are applied to enhance Optical Coherence Tomography Angiography (OCTA) images. SK operators are sampling type operators that, due to their approximation properties, are particularly suitable for

© The Author(s), under exclusive license to Springer Nature Switzerland AG 2026
O. Gervasi et al. (Eds.): ICCSA 2025 Workshops, LNCS 15892, pp. 358–378, 2026.
https://doi.org/10.1007/978-3-031-97638-4_23

the reconstruction of digital images which are discontinuous signals (see, e.g., [22]). Throughout the article, the most significant theoretical results about these operators are presented. The benefits related to their implementation result in a reconstruction of the image characterized by a rescaling, which produce an enhancement of its informational content, and simultaneously a reduction of noise, by attenuating high frequencies. The remarkable reconstruction capabilities of SK operators have also been useful in other applications (see, e.g., [7,20,21,40]). Basing on these peculiarities, this study aims to leverage the potential of SK operators to improve the quality of OCTA images, thereby supporting the analysis and diagnosis of retinal pathologies.

In recent years, Optical Coherence Tomography Angiography has become a pivotal diagnostic tool in ophthalmology, providing detailed images of retinal layers through a non-invasive procedure. Given the retina's crucial role in vision, in-depth examinations are necessary for managing diseases such as diabetic retinopathy (DR), a common complication of diabetes mellitus and a leading cause of blindness in the working-age population worldwide (see e.g. [29]). Consequently, accurate diagnosis is essential to prevent vision loss. Although Fluorescein Angiography (FA) continues to be the gold standard diagnostic procedure for studying diabetic retinopathy, it is expensive, time-consuming, and invasive, as it requires the injection of contrast agents, which some patients may not tolerate well. Therefore, it is not suitable for the prevention of DR (see e.g. [8]). Conversely, Optical Coherence Tomography (OCT) and its extension, OCT Angiography (OCTA), have emerged as effective alternatives for preventing retinal diseases. This technique rapidly produces high-resolution images of blood flow across all retinal vascular layers without the necessity for contrast agents, unlike Fluorescein Angiography, which only visualizes the superficial plexus. Despite its advantages, OCTA has limitations such as artifacts caused by rapid eye movements and fluid presence. Over the years, various studies have focused on improving image quality and reducing noise in OCTA images (see e.g., [35,37]). For instance, a study on OCTA images of healthy patients was conducted in [14], and later extended to diabetic patients in [39] due to their propensity for developing retinal diseases such as diabetic retinopathy (see e.g. [36]). These studies focused on images of the superficial capillary plexus (SCP) and choriocapillary plexus (CC), which were directly obtained from OCTA exams, taking advantage of the ability to visualize different layers of the retina. High-resolution images from OCTA enable visualization of DR features such as microaneurysms, neovascularizations, and impacts on foveal avascular zone (FAZ) morphology. As highlighted in [18], OCTA's strength lies in its ability to detect early-stage effects of diabetic retinopathy.

This study evaluates a method for the reconstruction of digital images using tools from Approximation Theory. Specifically, OCTA images from 17 clinically healthy patients and 15 diabetic patients were pre-processed through double registration and averaging processes, followed by the reconstruction using an algorithm based on Sampling Kantorovich (SK) operators.

The first part of the present paper specifically focuses on comparing only averaged, from one side, versus averaged and then SK-reconstructed images.

These reconstructed images were examined using the Peak-Signal-to-Noise Ratio (PSNR) and Structural Similarity Index (SSIM), which are widely used similarity indices, calculated between OCTA and fluorescein angiography images, with the latter considered as the target. Additionally, the evaluation was performed by counting the number of connected components (i.e. the clusters) ([30]), as scientific evidence suggests that the retinal vessel network is ideally completely interconnected (see e.g. [14,34]). Another significant application of OCTA presented in this study is the analysis of the foveal avascular zone (FAZ), a capillary-free region at the center of the fovea, within the retina. After extracting the binary masks of the FAZ from SCP images reconstructed with the SK algorithm, various metrics, such as area, perimeter, circularity, axis ratio, eccentricity and orientation, were computed and analyzed to highlight the differences between healthy and diabetic patients. The shape and size of the FAZ are closely linked to the onset and progression of retinal conditions, highlighting the importance of OCTA examinations in monitoring patients with diabetic retinopathy (see e.g. [26,31]). The application of SK operators enabled the extraction of crucial information, thereby allowing for a precise evaluation of the considered metrics. To the best of the authors' knowledge, this is the first article proposing the analysis of the FAZ using reconstructed SCP images with an algorithm coming directly from the theoretical setting of Sampling Theory.

This paper is organized as follows: Sect. 2 reviews the mathematical setting and the most significant results regarding sampling Kantorovich operators.

Section 3 describes the methodology, including all the pre-processing steps and the description of the two main processes carried out, namely, the counting of clusters for averaged images and those additionally reconstructed using the SK algorithm. Then, we detail the process for identifying the FAZ area from the SK reconstructed SCP images and the subsequent extraction of metrics used for a quantitative evaluation of FAZ features between healthy and diabetic patients. Section 4 details the experimental data, while Sect. 5 provides an in-depth analysis of the outcomes for both procedures. Finally, we outline the conclusions.

2 Sampling Kantorovich Operators: Approximation Results and Implementation

Introduced in 2007 in [9] in the unidimensional setting and extended to the multidimensional context in 2011 in [23], sampling Kantorovich operators represent a significant mathematical tool in Sampling Theory. In order to recall the definition and approximation properties of these operators, preliminary concepts must be addressed.

Let $\Pi^n = (t_{\underline{k}})_{\underline{k}\in\mathbb{Z}^n}$ be a sequence defined by $t_{\underline{k}} = (t_{k_1},...,t_{k_n})$, where $(t_{k_i})_{k_i\in\mathbb{Z}}$, $i = 1,...,n$ is a sequence of real numbers for which $-\infty < t_{k_i} < t_{k_{i+1}} < +\infty$, $\lim_{k_i\to\pm\infty} t_{k_i} = \pm\infty$ for every $i = 1,...,n$ and such that there exist Δ, $\delta > 0$ for which $\delta \leq \Delta_{k_i} = t_{k_i+1} - t_{k_i} \leq \Delta$, for every $i = 1,...,n$.

Then, we call *kernel* (for the sampling Kantorovich operator) a function $\chi : \mathbb{R}^n \to \mathbb{R}$ that satisfies the following conditions:

(K1) $\chi \in L^1(\mathbb{R}^n)$ and is bounded in a neighbourhood of $\underline{0} \in \mathbb{R}^n$;
(K2) For every $\underline{u} \in \mathbb{R}^n$,

$$\sum_{\underline{k} \in \mathbb{Z}^n} \chi(\underline{u} - t_{\underline{k}}) = 1;$$

(K3) For some $\beta > 0$, the discrete absolute moment of order β is finite, i.e.

$$m_{\beta,\Pi^n}(\chi) = \sup_{\underline{u} \in \mathbb{R}^n} \sum_{\underline{k} \in \mathbb{Z}^n} |\chi(\underline{u} - t_{\underline{k}})| \cdot ||\underline{u} - t_{\underline{k}}||_2^{\beta} < +\infty.$$

For every $\underline{k} \in \mathbb{Z}^n$, and $w > 0$, the set defined as

$$R_{\underline{k}}^w = \left[\frac{t_{k_1}}{w}, \frac{t_{k_1+1}}{w}\right] \times \left[\frac{t_{k_2}}{w}, \frac{t_{k_2+1}}{w}\right] \times ... \times \left[\frac{t_{k_n}}{w}, \frac{t_{k_n+1}}{w}\right] \quad (w > 0)$$

is a subset of $\mathbb{R}^n$. Moreover, if we denote by $A_{\underline{k}} := \Delta_{k_1} \cdot ... \cdot \Delta_{k_n}$, then the Lebesgue measure of $R_{\underline{k}}^w$ is given by $\frac{A_{\underline{k}}}{w^n}$ and

$$\frac{\delta^n}{w^n} \leq \frac{A_{\underline{k}}}{w^n} \leq \frac{\Delta^n}{w^n}.$$

Definition 1. *Let χ be a kernel. The family of operators $(S_w^\chi)_{w>0}$ defined by*

$$(S_w^\chi f)(\underline{x}) = \sum_{\underline{k} \in \mathbb{Z}^n} \chi(w\underline{x} - t_{\underline{k}}) \cdot \left[\frac{w^n}{A_{\underline{k}}} \cdot \int_{R_{\underline{k}}^w} f(\underline{u}) d\underline{u}\right] \quad \underline{x} \in \mathbb{R}^n, \tag{1}$$

where $f : \mathbb{R}^n \to \mathbb{R}$ is a locally integrable function, and the series converges for each $\underline{x} \in \mathbb{R}^n$, is known as the multivariate sampling Kantorovich operator, or briefly SK-operator.

SK operators represent a generalization of the generalized sampling operators introduced by P.L. Butzer in [11], as their definition allows for the reconstruction of signals that are not necessarily continuous. This peculiarity enables the reconstruction of digital images, which are two-dimensional discontinuous signals. In what follows we report some approximation results, proven in [23], whose implementation allows the reconstruction and the enhancement of the images by means of SK operators.

In particular, when dealing with continuous signals, the following convergence result holds.

Theorem 1. *Let $f \in C^0(\mathbb{R}^n)$. Then, for every $\underline{x} \in \mathbb{R}^n$,*

$$\lim_{w \to +\infty} (S_w^\chi f)(\underline{x}) = f(\underline{x}).$$

In particular, if $f \in C(\mathbb{R}^n)$, then

$$\lim_{w \to +\infty} ||S_w^\chi f - f||_\infty = 0,$$

where $C(\mathbb{R}^n)$ (resp. $C^0(\mathbb{R}^n)$) denotes the space of uniformly continuous and bounded (resp. continuous and bounded) functions on $\mathbb{R}^n$.

Another noteworthy outcome shows that it is possible to reconstruct by the SK operators even not-necessarily continuous signals. Indeed, the following L^p-convergence theorem holds.

Theorem 2. *For every $f \in L^p(\mathbb{R}^n)$, $1 \leq p < +\infty$, the following estimate holds:*

$$||S_w^\chi f||_p \leq \delta^{-n/p}(m_{0,\Pi^n}(\chi))^{(p-1)/p}||\chi||_1^{1/p}||f||_p \quad (f \in L^p(\mathbb{R}^n)),$$

showing that the operator maps $L^p(\mathbb{R}^n)$ into $L^p(\mathbb{R}^n)$, and

$$\lim_{w \to +\infty} ||S_w^\chi f - f||_p = 0.$$

In addition to convergence, various other significant properties of sampling Kantorovich operators have been investigated, such as regularization, saturation, and inverse results (see, for example, [5,24]). The kernel, which is the function satisfying conditions **(K1)**–**(K3)**, plays a pivotal role in the study and implementation of SK operators.

Literature provides numerous examples of kernels, some of which are described below. In the reconstruction algorithm undertaken in this work, the *Jackson-type kernels* were selected for the SK operators. These are a class of product-type (tensor product) multivariate kernels (see e.g. [13]), defined as:

$$\mathcal{J}_k^n(\underline{x}) = \prod_{i=1}^{n} J_k(x_i), \quad \underline{x} \in \mathbb{R}^n,$$

in which

$$J_k(x) = c_k sinc^{2k}\left(\frac{x}{2k\pi\alpha}\right)$$

are the one-dimensional Jackson-type kernels, with $x \in \mathbb{R}$, $k \in \mathbb{N}$, $\alpha \geq 1$, where

$$sinc(x) := \begin{cases} \frac{sin(\pi x)}{\pi x} & x \in \mathbb{R} \setminus \{0\} \\ 1 & x = 0, \end{cases}$$

and c_k is a non-zero normalization coefficient given by

$$c_k := \left[\int_{\mathbb{R}} sinc^{2k}\left(\frac{u}{2k\pi\alpha}\right) du\right]^{-1}.$$

See Fig. 1.a for a graphical representation.

Another category of product-type kernels includes the well known *Fejer' kernels*, defined as

$$\mathcal{F}_n(\underline{x}) = \prod_{i=1}^{n} F(x_i)$$

where

$$F(x) := \frac{1}{2} sinc^2\left(\frac{x}{2}\right) \quad (x \in \mathbb{R})$$

is its one-dimensional version. The bidimensional graphical representation of this kernel can be seen in Fig. 1.b. Other multivariate kernels, which are not of the product type, include radial-type kernels. For instance, we mention the *Bochner-Riesz kernels* which are defined as

$$b_n^{\alpha}(\underline{x}) := 2^{\alpha}\Gamma(\alpha+1)||\underline{x}||_2^{-(n/2+\alpha)}B_{(n/2+\alpha)}(||\underline{x}||_2),$$

for $\underline{x} \in \mathbb{R}^n$ and where $\alpha > \frac{n+1}{2}$, B_λ is the Bessel function of order λ and Γ is the Euler function, see Fig. 1.c for its graph. For more details about kernels, see e.g. [12,13].

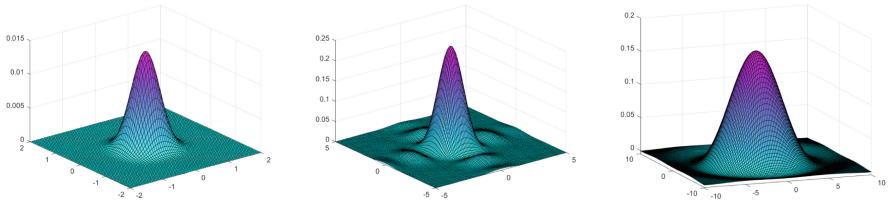

(a) Jackson J_2^2 (b) Fejer $\mathcal{F}_2$ (c) Bochner-Riesz b_2^2

Fig. 1. Graphs of the previously mentioned bidimensional kernels. Specifically, the Jackson-type kernel is shown in image (a), Fejer's kernel in image (b), and Bochner-Riesz's kernel in image (c).

Due to the distinctive properties of the sampling Kantorovich operators, digital images can be reconstructed by such operators, improving their quality. A grey scale image can be modeled as a matrix $A = (a_{ij})_{i,j=1,\dots,m}$ that can be represented by a step function $I \in L^p(\mathbb{R}^2)$, with $1 \leq p < +\infty$.

In particular,

$$I(x,y) := \sum_{i=1}^{m}\sum_{j=1}^{m} a_{ij} \cdot \mathbf{1}_{ij}(x,y) \qquad (x,y) \in \mathbb{R}^2$$

where

$$\mathbf{1}_{ij}(x,y) = \begin{cases} 1, & if \quad (x,y) \in (i-1,i] \times (j-1,j], \\ 0, & otherwise. \end{cases}$$

Hence it is possible to reconstruct I by means of the operator (1) in its two-dimensional form and selecting a previously described kernel. Therefore, notable results are achieved: firstly, the image is resized according to a selected rescaling factor R. Additionally, owing to the convolutive nature of the operator, it also acts as a smoothing filter, thereby attenuating any noise present in the image. Consequently, the result is a new image with enhanced informational content based on the chosen parameters. One of these is the sampling rate. This, in particular, allows for practical observation of the theoretical approximation

results discussed in this section. In Theorems 1 and 2, the convergence of the operator to the signal as w increases is established; therefore, in practice, a higher sampling rate results in a more accurate image reconstruction. This procedure has been implemented in Matlab, see e.g. [21] for the pseudo-code of the algorithm. The latter has been evaluated in performance and with respect to the CPU time, proving greater efficiency compared to other interpolation and quasi-interpolation algorithms known in literature (see [22]). Finally, we highlight that, beyond the classic SK operators, other types of sampling operators and their modifications can be found in literature (see e.g., [1–4,16,19,41]).

3 Methodology

Optical Coherence Tomography Angiography (OCTA) is an innovative and clinically significant imaging technique for examining retinal and sub-retinal vasculature. This modality relies on repeated scans to detect motion and identify blood vessels based on changes in signal reflection caused by blood flow. Variations in flow speed and patient movements can introduce noise and artifacts. To address these issues, averaging multiple en face OCTA images can reduce noise, improve vascular continuity, and enhance both qualitative and quantitative evaluations (see e.g. [35,37]).

In our study, sequences of images related to the superficial capillary plexus (SCP) and the corresponding choriocapillaris (CC) images undergo two separate registration processes to ensure perfect image alignment. The SCP acquisition with the lowest noise was chosen as the reference for the registration process, and consequently, the corresponding CC image was used as the reference for the CC layer, considering that the CCs are rigidly connected with the corresponding SCPs (see e.g. [14,39]).

First, images undergo affine registration using the *Fiji* plugin *Turboreg* (see, e.g. [38]). Throughout this process, the source image is adjusted with rigid body deformations, translations, and rotations to minimize the Mean Square Error (MSE) between the source and target images; MSE is a similarity index between two $M \times N$ images, namely, $I_A(i,j)$ and $I_B(i,j)$, defined as:

$$MSE = \sum_{i=1}^{M} \sum_{j=1}^{N} \frac{|I_A(i,j) - I_B(i,j)|^2}{MN}. \tag{2}$$

Due to the organic composition of the eye, which includes tissues and fluids, accurate alignment requires a secondary registration. This involves the application of landmark-based registration. Initially, the *Extract MOPS Correspondences* plugin is used to extract features (see e.g. [10]), followed by the *bUnwarpj* plugin (see e.g. [6]). This method is applied to all SCP images for each patient, aligning them with the selected least noisy image used as the target. For the CC images, the sequences are registered using the correspondent CC of the SCP target as the reference, with the coordinates from the latter image transferred.

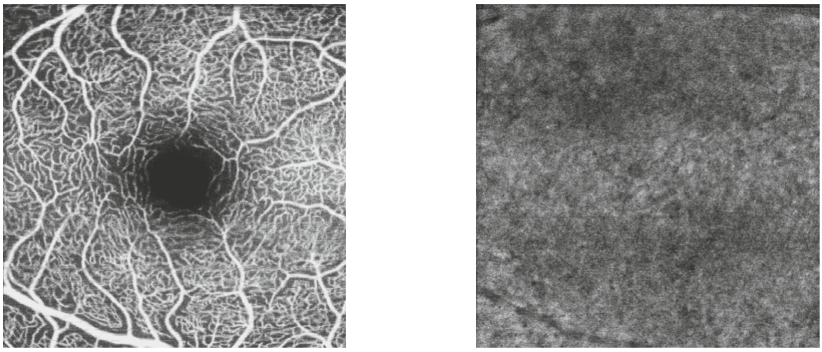

Fig. 2. Example of SCP (left) and CC (right) exams after the registration and averaging process.

Subsequently, each sequence undergoes averaging to reduce noise, resulting in a single SCP and a single CC image per patient, as illustrated in Fig. 2.

At this point, images are reconstructed using the SK algorithm, as described in the previous section. The implementation is performed with a two-dimensional Jackson-type kernel, setting $k = 12$ and a rescaling factor $R = 2$.

3.1 Cluster Counting Process

Scientific evidence indicates that the retinal tree is highly interconnected, resulting ideally in a unique connected component (see e.g. [14]). Therefore, to count clusters identifying retinal vascularization in OCTA images, it is necessary to implement a segmentation procedure for both SCP and CC images. For SCP images, a hybrid thresholding process was applied ([14]), combining the Otsu method ([32]) and the Phansalkar technique ([33]). This approach aims to achieve suitable thresholding in each image region, avoiding over-segmentation in uniform areas caused by Otsu and the risk of over-connecting vessels typical of Phansalkar. The latter technique is applied in the macula area, while Otsu is used for the rest of the image. The final thresholded image ($I_T(i,j)$) is defined as the logical AND ($\wedge$) of the image thresholded with Phansalkar ($B_P(i,j)$) and the one thresholded with Otsu ($B_O(i,j)$):

$$I_T(i,j) = B_P(i,j) \wedge B_O(i,j), \quad i = 1,2,...,N; \; j = 1,2,...,M. \tag{3}$$

For CC images, the Phansalkar method is applied as it is particularly suitable for low-contrast images, such as those depicting the choriocapillaris layer (see e.g. [39]). This procedure was applied with a radius of 7 pixels for the averaged images and 15 pixels for averaged images reconstructed with the SK algorithm. For the count of the connected components (i.e., the clusters) on the thresholded images was performed the plugin *Find Connected Regions* of Fiji, exploiting the 8-adjacency criterion. The plugin can provide information on the connected components found, such as their size and area. In Fig. 3 we can appreciate an

example of the clusters localization for both the SCP and CC images. This segmentation procedure and the application of the plugin was conducted on both averaged images and those averaged and reconstructed with the SK algorithm, to compare and evaluate the advantages of the reconstruction with the sampling Kantorovich operators in the cluster counting process.

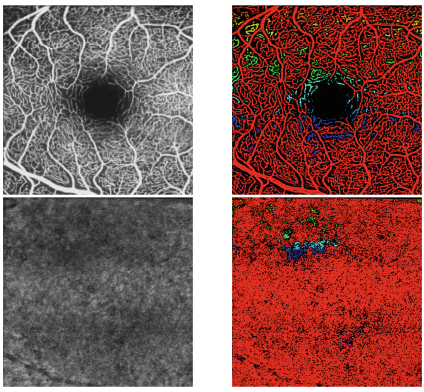

Fig. 3. Examples of SCP images (top left) and CC images (bottom left) along with their respective cluster counting results after applying the plugin to the thresholded images.

3.2 Extraction of FAZ Metrics

Analyzing the foveal avascular zone (FAZ) is another important application of OCTA. Studies have shown that various FAZ metrics, such as area, perimeter, circularity, axis ratio, eccentricity and orientation change in relation to different diseases. These metrics could serve as effective indicators for monitoring disease progression, especially diabetic retinopathy, see e.g. [8,15,26,31]. Then, identifying early biomarkers of diabetic changes in the ocular fundus is crucial for slowing the progression of this condition. With this aim, segmenting the FAZ in the SCP layer aids in quantifying these parameters. While FAZ measurements have traditionally been manual, recent automated algorithms reduce subjectivity and expedite analysis (see, e.g., [17]). In this study, we use SCP images reconstructed with the SK algorithm for the extraction of the FAZ, in order to take advantage of the increased information and attenuated noises, coming from the reconstruction, to compute the parameters chosen for the analysis. The extraction of the FAZ is made with the *Level Sets* plugin from Fiji (see e.g. [43]). This plugin is semi-automatic and involve two methods based on PDE, in particular we choose the one called *Active Contours*, that deforms iteratively the initial seed defined by the user to adapt to object contours, producing binary masks like the one we see in Fig. 4, where the FAZ is highlighted in white.

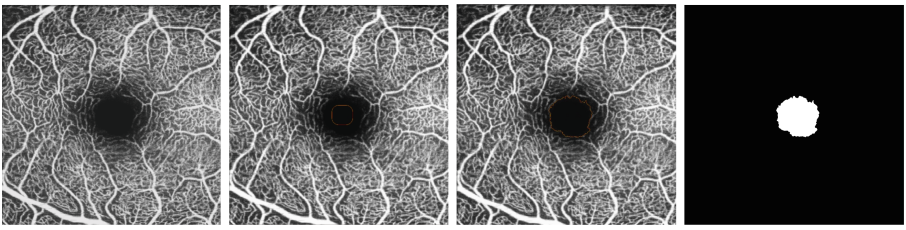

Fig. 4. Starting from the left we have the SCP image and two expansions of the seed with the plugin. Then, the fourth image display the final binary mask showing the FAZ, as outcome of the application of *Level Sets*.

Following the acquisition of the binary mask outlining the FAZ region, metrics are extracted to evaluate its dimensions and morphology. The MATLAB *regionprops* function ([44]) is used for this purpose. Various properties are measured for the connected component of the image, including *area, perimeter, circularity, axis ratio, eccentricity,* and *orientation*. Area represents the number of pixels composing the FAZ, while perimeter is computed using a method based on chain coding (see e.g. [25]).

Circularity is calculated with the formula

$$C = \frac{4\pi A}{P^2},$$

where A denotes the area and P the perimeter. This metric approaches zero as the shape becomes less rounded or smooth.

The axis ratio is defined as the ratio between the major and minor axes of the ellipse with the same second central moment (see e.g. [27]) as the FAZ region (see Fig. 5), always greater or equal to 1,

$$Axis\ ratio = \frac{Major\ axis}{Minor\ axis} \geq 1,$$

see e.g. [28]. Eccentricity, also referring to the ellipse with the same second central moment as the region, is a scalar value defined as the ratio between the distance of the ellipse's foci (F_1, F_2) and the length of its major axis:

$$Eccentricity = \frac{d(F_1, F_2)}{MajorAxis}.$$

It ranges from zero (indicating a circle) to one (indicating a line segment). The final metric, orientation, is defined as the angle between the x-axis and the major axis of the ellipse, with values ranging from $-90°$ to $90°$. See Fig. 5 for a visual representation of the parameters used to extract these metrics.

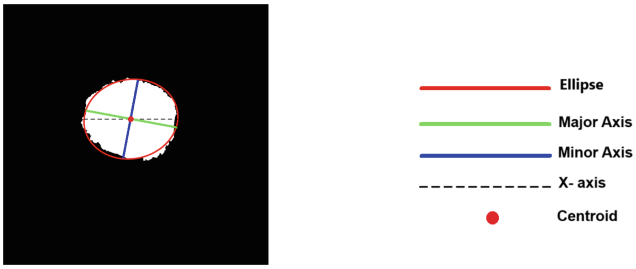

Fig. 5. Example of FAZ area in which are superposed the correspondent ellipse (in red) with the same second central moment, the major axis (in green), the minor axis (in blue) and the centroid (the red point). (Color figure online)

4 Experimental Data

The above procedure was conducted on 32 images from 32 different eyes. Specifically, 17 of these images belong to clinically healthy patients with no known eye diseases; therefore, they will represent the so called *control group*. The other 15 images are from patients with diabetes. This choice is based on the fact that diabetic patients often develop eye diseases, as previously mentioned.

The dataset was collected at the Santa Maria della Misericordia Hospital in Perugia, using the SPECTRALIS HRA+OCT2 (Heidelberg Engineering, Heidelberg, Germany) for the examinations. This device can perform 85,000 A-scans per second, achieving an axial resolution of 3.9µm and a lateral resolution of $6\mu m$. It uses an algorithm for probabilistic amplitude decorrelation and an 870nm light source with a 50nm bandwidth. TruTrack®Active Eye Tracking Technology was employed to minimize motion artifacts. The acquisitions were conducted using the high-resolution preset, involving a $10° \times 10°$(3.1mm × 3.1mm) − 15° angle volume scan (512 B-scans with 6µmm spacing between consecutive B-scans, using an averaging technique of 5 frames per scan) centered in the foveal region. En-face angiograms were analyzed using the viewer software (Heyex Software, version 1.9.201.0, Heidelberg Engineering, Heidelberg, Germany). For each patient, the OCTA scan acquired five SCP images and five CC images with short intervals between each acquisition. All images have been anonymized and converted into 8-bit images.

5 Numerical Results

This section presents the results from the two procedures described before: a qualitative analysis comparing averaged images (AVG) with those averaged and processed using the Sampling Kantorovich algorithm (AVG+SK), and an analysis of the FAZ to evaluate morphological differences between healthy and diabetic patients.

5.1 Cluster Counting Process

The objective of this part of the study is to evaluate the reconstruction capabilities of the sampling Kantorovich algorithm, applied to OCTA images. For the evaluation, we have calculated the number of connected components (i.e., the clusters) of the images. Before delving into this point, we present an initial evaluation of the SK algorithm applied to the averaged (AVG) and reconstructed (AVG+SK) SCP images, compared with two available fluoroangiographic images from two diabetic patients in our dataset; the comparison with healthy patients has been already done in [14]. For the evaluation, we considered three similarity indices known in literature: PSNR, MSE, and SSIM. The MSE was already defined in (2) of Sect. 3, while PSNR, that is the Peak Signal to Noise Ratio, is defined as

$$PSNR = 10 \cdot \log_{10}\left(\frac{(f_{max})^2}{MSE}\right)$$

where f_{max} is the maximum value of the image. Regarding SSIM (see e.g. [42]), this is a widely appreciated similarity index that compares images under three aspects: luninance, contrast and structural features. Evaluated between two images X and Y of the same size, it gives a value in $[-1, 1]$, approaching to 1 when the images coincide, 0 when there is no correlation between the two images, and -1 where there is perfect anti-correlation. It is defined as follows:

$$\begin{aligned} SSIM(X,Y) &= l(X,Y) \cdot c(X,Y) \cdot s(X,Y) \\ &= \frac{(2\mu_X\mu_Y + C_1)(2\sigma_{XY} + C_2)}{(\mu_X^2 + \mu_Y^2 + C_1)(\sigma_X^2 + \sigma_Y^2 + C_2)}. \end{aligned}$$

Here, μ_X and μ_Y are the mean of the intensity values of the respective images, σ_X^2, σ_Y^2 are the variances of the images X and Y, σ_{XY} is the covariance between X and Y, and C_1, C_2 are constants to prevent instability.

Table 1. Comparison of AVG versus AVG+SK methods for SCP and fluoroangiographic images of diabetic patient number 6 and 7, using PSNR, MSE, and SSIM indices.

Diabetic Eye Nr.	Method	PSNR	MSE	SSIM	Img. Pixels
6	AVG	11.5599	4540.4	0.2266	883600
6	AVG+SK	11.6061	4492.3	0.2346	883600
Diabetic Eye Nr.	Method	PSNR	MSE	SSIM	Img. Pixels
7	AVG	11.6210	4476.9	0.3957	883600
7	AVG+SK	11.6610	4435.2	0.4059	883600

From Table 1, we observe that the reconstruction using the SK algorithm (AVG+SK) yields better PSNR, MSE, and SSIM values compared to the averaged image alone (AVG). For this comparison, the AVG+SK images were reconstructed with the SK algorithm using a sampling rate of $w = 20$ and a scaling

factor of $R = 1$, to avoid altering the target. It is important to note that this evaluation involves images acquired through two different methods: one SCP from OCTA and one fluoroangiographic. Therefore, excessively high results are not expected in these evaluations. Among the three indices, SSIM provides a more objective comparison as it evaluates images based on stricter characteristics compared to the other indices (see [42] for further details). The improved SSIM value in the evaluation between SCP and fluoroangiography in the patient's images highlights that the SK algorithm effectively reconstructs the SCP image, making it more similar to the target, which is the fluoroangiography image. We conducted tests with different sampling rates and consistently obtained better results for all three indices in the AVG+SK reconstructed images with respect to the only averaged images (AVG). Therefore, we can conclude that the SK algorithm, when applied to OCTA images, enhances their quality and increases the informational content for studying retinal pathologies.

As previously mentioned, the vascular network in SCP and CC images can ideally be considered fully connected. Therefore, a decrease in the number of clusters indicates good results. The clusters counting procedure was applied to both the averaged images and those averaged and reconstructed with the SK algorithm for comparison purposes. A preliminary study in this direction was conducted in [14]. The tables show the results (mean values) over the 17 clinically healthy patients and the 15 diabetic patients of the clustering counting process for healthy eyes (in Tables 2 and 4) and diabetic eyes (in Tables 3 and 5).

From the tables, it is evident that the mean values number of clusters in SK reconstructed images is lower compared to those without its application, both in SCP and CC images, indicating that the SK algorithm more accurately reconstructs the retinal vasculature by significantly reducing noise and vessel discontinuities. This improvement is reflected in the increased area of clusters in the reconstructed images and is consistent for both diabetic patients and the control group. In each table, data are organized as follows: the type of patient; the method used for image processing (AVG = only averaged, $AVG + SK$ = averaged and reconstructed using the SK algorithm); the number of clusters (Nr. Clusters); the mean cluster area (Mean Area, in pixels) and its standard deviation (St. Dev. Area in pixel). The area and standard deviation values are scaled according to the image size for comparison. Cluster analysis indicates stronger vessel connections in images processed with the SK algorithm, applicable to both SCP and CC layers. Variations in image size do not impact the analysis results, as the area measurements are adjusted according to pixel count. However, larger images tend to have more clusters, therefore images reconstructed with the SK algorithm are more reliable, showing fewer connected regions even in larger images, compared to those only averaged. Exams of diabetic patients generally show a higher average number of clusters than those of healthy individuals, highlighting the disease's effect on retinal conditions.

Table 2. Data from SCP healthy eyes.

SCP Healthy Eyes	Method	Nr. Clusters	Mean Area	St. Dev. Area
Mean	AVG	1643.4	249.8	7825.8
Mean	$AVG + SK$	1271.9	331.3	9104.4

Table 3. Data from SCP diabetic eyes.

SCP Diabetic Eyes	Method	Nr. Clusters	Mean Area	St. Dev. Area
Mean	AVG	2480.7	139.7	3214.3
Mean	$AVG + SK$	2041.4	161.8	3180.5

Table 4. Data from CC healthy eyes.

CC Healthy Eyes	Method	Nr. Clusters	Mean Area	St. Dev. Area
Mean	AVG	554.6	1979.9	35075.1
Mean	$AVG + SK$	343.9	4138.5	48734.0

Table 5. Data from CC diabetic eyes.

CC Diabetic Eyes	Method	Nr. Clusters	Mean Area	St. Dev. Area
Mean	AVG	2999.7	708.1	15275.0
Mean	$AVG + SK$	2105.3	1321.6	22383.5

5.2 FAZ Analysis

As previously mentioned, the size and shape of the FAZ are linked to conditions such as aneurysms, capillary loss, and ischemia. Therefore, measuring FAZ metrics is essential for diagnosing and monitoring retinal vascular diseases, including diabetic retinopathy and retinal vein occlusion. Given that diabetic retinopathy is a leading cause of blindness and the number of diabetic patients is expected to rise (see e.g., [29]), a thorough analysis of the relationship between disease progression and key markers could be medically advantageous. After extracting the FAZ area from the SCP images, which were averaged and reconstructed using the SK algorithm, the metrics under evaluation include area, perimeter, circularity, axis ratio, eccentricity, and orientation. These metrics were extracted using MATLAB's function *regionprops*. Tables 6 and 7 present the results for the FAZ of each patient, along with the mean and standard deviation for every metric. From an initial assessment of the individual metrics, it is evident that healthy patients exhibit more constricted and more circular FAZ. To conduct a more in-depth evaluation, Fig. 6 presents the boxplots of each metric for healthy and diabetic patients. These graphs are particularly suitable for our study as they offer an intuitive insight into the distributions of the two populations, even when their cardinalities differ, as in our case. The boxplots illustrate the extreme val-

ues of the population (maximum and minimum), the interquartile range (the width of the box), the median (highlighted in blue), and any potential outliers.

From the boxplots, it is evident that the FAZ metrics for the control group exhibit a more concentrated and less variable distributions compared to those of diabetic patients. This is deduced from the extent of the boxplots, which are more concentrated for the control group, despite some outliers representing exceptional cases.

Specifically, the area and perimeter values are smaller for healthy individuals, with respective mean values of 112224 and 1471.19 pixels, highlighting more extensive avascularization in the diabetic group, which has mean values of 160659 pixels and a perimeter of 2135.25 pixels. Additionally, the length of the boxplots indicates that the distribution of values is less variable for healthy individuals compared to diabetics, especially for the FAZ perimeter which has a clearly smaller inter-quartile range. Regarding circularity, the control group shows a concentration of values overall closer to one, associated with a circular shape of the FAZ, in contrast to the significantly higher variability observed in diabetic patients, with a notably wider range of values. This is evident from the standard deviation, with values of 0.0910 and 0.176 for the healthy and diabetic groups, respectively.

In line with the previous deductions regarding the shape, the axis ratios for the FAZs of healthy individuals are concentrated around one with a uniform distribution around the median. The variability distribution of the two groups is also evident from the standard deviation, which is 0.067 for healthy patients and 0.820 for diabetics. These two metrics suggest that the FAZs of healthy individuals have more regular and circular shapes, while those of diabetic patients display more variable and irregular widening, maybe related to the progression stage of the pathology, as evidenced by the greater variability in the data.

This observation is further supported by the eccentricity values, which indicate a more regular elliptic shape, occasionally approaching a perfect circle (see the red point, i.e., the outlier), in the FAZs of healthy individuals.

Regarding the orientation metric, it is observed that for the control group, the angle between the major axis and the horizontal line is around $0 \pm 15°$ for more than 50% of the values, notable from the median and the inter-quartile range, whereas the diabetic group shows a wide variation. This result aligns with the findings in [26], where lower variability in orientation values is noted for patients without any disease, with angles close to $0°$ or $90°$.

From the results shown in the previous Tables 6 and 7 and Fig. 6 we can assert that diabetic pathology induces alterations in the FAZ region, as evidenced by the proposed metrics. Therefore, it is evident that the assessment of area, perimeter, circularity, axis ratio, eccentricity, and orientation can serve as valid tools for evaluating the progression of diabetic retinopathy and the development of potential complications such as diabetic macular edema.

Table 6. FAZ metrics, and the respective means and standard deviations, of healthy patients. In particular, area and perimeter are expressed in pixels, circularity, axis ratio and eccentricity are dimensionless while orientation is expressed in degrees.

Healthy Eye N.	Area	Perimeter	Circularity	Axis Ratio	Eccentricity	Orientation
1	117813	1805.0	0.4544	1.0959	0.4090	13.7793
2	82649	1186.9	0.7373	1.1273	0.4616	5.6468
3	137892	1489.6	0.7809	1.1243	0.4570	14.6611
4	70800	1216.3	0.6014	1.1757	0.5259	4.6793
5	102866	1587.9	0.5127	1.1501	0.4939	7.6333
6	97632	1398.5	0.6273	1.1072	0.4293	30.1757
7	271920	2290.2	0.6515	1.1918	0.5440	−10.5787
8	142489	1652.2	0.6559	1.2278	0.5802	6.6129
9	132030	1664.0	0.5992	1.2177	0.5706	13.8743
10	117494	1441.8	0.7102	1.0274	0.2295	−4.3935
11	86953	1253.8	0.6950	1.1631	0.5106	−0.7963
12	33236	870.6	0.5511	1.0482	0.2999	−22.5476
13	97251	1406.2	0.6180	1.0918	0.4015	−31.0085
14	97630	1356.8	0.6664	1.0922	0.4021	−27.9770
15	147060	1615.0	0.7085	1.1968	0.5494	−7.6721
16	101054	1392.7	0.6547	1.0090	0.1336	80.0086
17	71037	1382.4	0.4671	1.0437	0.2862	−44.7690
Mean	112224	1471.19	0.6289	1.1229	0.4285	1.6075
Std. Dev.	50478	303.94	0.0910	0.0670	0.1270	27.9159

Table 7. FAZ metrics, and the respective means and standard deviations, of diabetic patients. The units of measurements are the same as Table 6.

Diabetic Eye N.	Area	Perimeter	Circularity	Axis Ratio	Eccentricity	Orientation
1	185424	2448.1	0.3888	1.3679	0.6823	12.5882
2	119932	1831.6	0.4492	1.1342	0.4718	14.4372
3	152281	1738.5	0.6329	1.2368	0.5885	−19.9861
4	141737	2073.1	0.4144	1.4314	0.7155	−80.8101
5	48088	1125.2	0.4773	1.1944	0.5468	−41.8157
6	225384	2109.3	0.6366	1.1746	0.5246	77.0606
7	364888	4549.5	0.2215	1.2208	0.5736	0.0139
8	154473	1697.4	0.6737	1.2562	0.6052	−14.0022
9	198093	2662.6	0.3511	1.4332	0.7164	−74.2340
10	88634	2493.8	0.1791	4.3929	0.9737	−85.9828
11	134646	1601.8	0.6595	1.2863	0.6289	−1.6377
12	82905	1147.0	0.7919	1.0366	0.2635	45.0435
13	241042	2391.6	0.5295	1.1801	0.5310	0.3111
14	114921	2183.7	0.3028	1.4522	0.7251	11.8383
15	157430	1975.2	0.5071	1.1159	0.4438	−45.3254
Mean	160659	2135.25	0.4810	1.4609	0.5993	−13.500
Std. Dev.	77082.8	808.59	0.1760	0.8200	0.1590	45.962

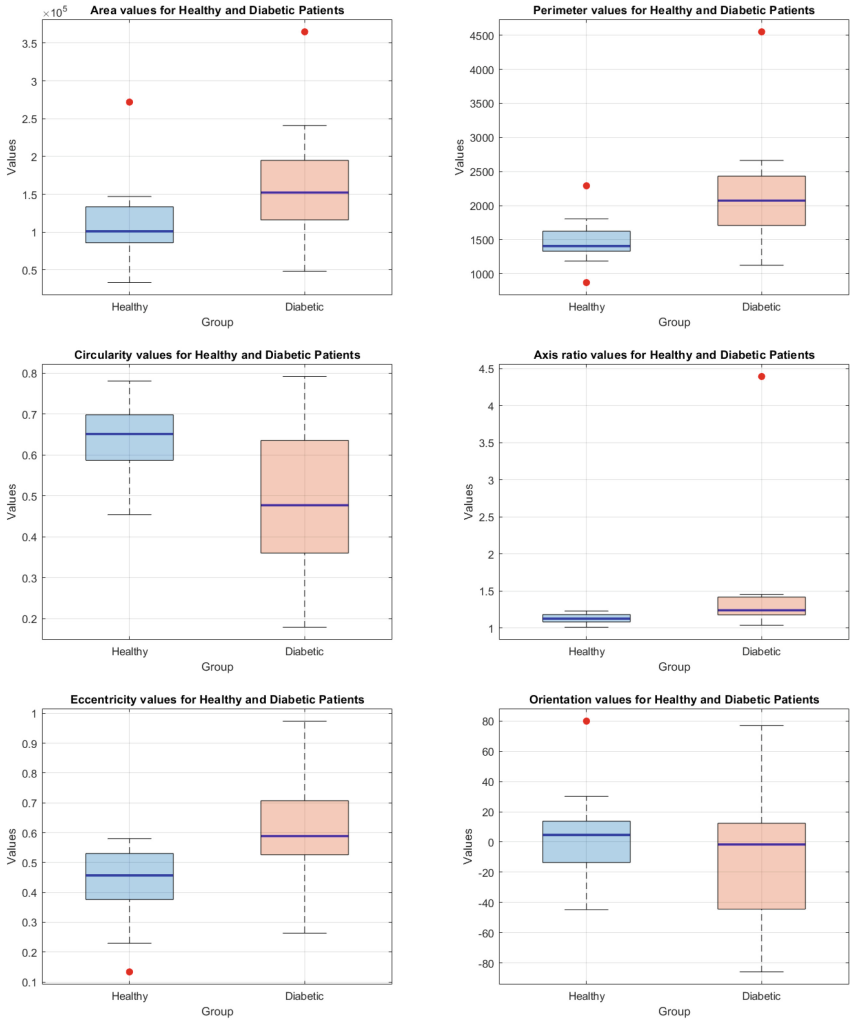

Fig. 6. Boxplot for each FAZ metric, comparing healthy patients (blue) and diabetic patients (orange). Outliers are shown in red, and median values are highlighted in blue. (Color figure online)

6 Conclusions

This paper introduces several innovations in the analysis of OCTA images. Previous studies have demonstrated that the application of the SK algorithm improves the quality of ocular fundus images (see e.g., [14,39]). Specifically, processed images have been shown to be overall more similar to target fluoroangiographic images, and thus more accurate compared to simply averaged ones. Furthermore, the cluster counting process in this paper shows that the SK algorithm improves

the representation of the vessel network by acting as a low-pass filter, reducing high-frequency noise. This results in a lower number of clusters, which is associated with a more connected vascular network. This improvement is observed in both healthy and diabetic individuals, the latter being more susceptible to eye diseases, like retinopathy. The observed variation in cluster counts between healthy and diabetic patients provides a basis for analyzing differences in eye perfusion between these groups. Therefore, the application of the SK reconstruction significantly enhances image quality, leading to improved medical diagnoses of eye diseases. In the latter part of the paper, binary masks of the foveal avascular zone were extracted from the SK-reconstructed SCP images to compute various metrics. These metrics highlighted significant variability between diabetic patients and the control group. Consequently, parameters such as area, perimeter, circularity, axis ratio, eccentricity, and orientation of the FAZ can be useful for disease prevention, complication monitoring, and follow-up. In this section of the study, the SK algorithm also plays a crucial role, enhancing the images from which the FAZ is extracted and thereby enabling the extraction of valuable information for metric computation. While the current dataset allowed for this analysis, a longitudinal study of the same patients from the onset of pathology would be interesting to observe how these parameters evolve as diabetes progresses, thereby minimizing interpersonal variability.

Acknowledgments. The authors wish to thank the Santa Maria della Misericordia Hospital of Perugia and the Ophtamology Section of the Department of Medicine and Surgery of the University of Perugia for kindly allowing the use of the images employed in this work.

Funding Information. The third and the fourth author have been supported within the project "Mathematical Methods and Models for Biomedical Applications" financied by National Recovery and Resilence Plan PNRR-III-C9-2022-I8.

Informed Consent Statement. All the images used are completely anonymized and it is not possible to trace the patients from the data mentioned in the paper.

Conflict of Interest/Competing Interests. The authors declare that they have no conflict of interest and competing interest.

Availability of Data and Material and Code Availability. Not applicable.

References

1. Acu, A.M., Aral, A., Raşa, I.: Generalized Bernstein Kantorovich operators: Voronovskaya type results, convergence in variation. Carpathian J. Math. **38**(1), 1–12 (2022)
2. Acu, A.M., Çetin, N., Tachev, G.: Approximation by perturbed Baskakov-type operators. J. Math. Inequalities **18**(2), 551–563 (2024)
3. Acu, A.M., Hodis, L., Rasa, I.: Multivariate weighted Kantorovich operators. Math. Found. Comput. **3**(2), 117–124 (2020)

4. Acu, A.M., Raşa, I.: New estimates for the differences of positive linear operators. Numerical Algorithms **73**(3), 775–789 (2016). https://doi.org/10.1007/s11075-016-0117-8
5. Angeloni, L., Çetin, N., Costarelli, D., Sambucini, A.R., Vinti, G.: Multivariate sampling Kantorovich operators: quantitative estimates in Orlicz spaces. Construct. Math. Anal. **4**(2), 229–241 (2021)
6. Arganda-Carreras, I., Kybic, J., Ortíz-de-Solórzano, C., Sorzano, C.O.: bUnwarpj: consistent and elastic registration in Imagej. In: Methods and applications, Second ImageJ User and Developer Conference, vol. 12 (2008)
7. Asdrubali, F., et al.: Detection of thermal bridges from thermographic images by means of image processing approximation algorithms. Appl. Math. Comput. **317**, 160–171 (2018)
8. Avila, M., De Barros Garcia, J.M.B., Isaac, D.L.C.: Diabetic retinopathy and OCT angiography: clinical findings and future perspective. Int. J. Retina Vitreous **3**(14), 1–10 (2017)
9. Bardaro, C., Vinti, G., Butzer, P.L., Stens, R.L.: Kantorovich-type generalized sampling series in the setting of Orlicz spaces. Sampling Theory Sig. Image Process. **6**(1), 29–52 (2007). https://doi.org/10.1007/BF03549462
10. Brown, M., Szeliski, R., Winder, S.: Multi-image matching using multi-scale ORI ENTED patches. In: Proceedings of the 2005 IEEE Computer Society Conference on Computer Vision and Pattern Recognition, vol. 1, pp. 510–517 (2005)
11. Butzer, P.L.: A survey of the Whittaker-Shannon sampling theorem and some of its extensions. J. Math. Res. Exposition **3**, 185–212 (1983)
12. Butzer, P.L., Fisher, A., Stens, R.L.: Generalized Sampling Approximation of Multivariate Signals: Theory and Some Applications, Note di Matematica, pp. 173–191 (1990)
13. Butzer, P.L., Nessel, R.J.: Fourier Analysis and Approximation I. Academic Press, New York-London (1971)
14. Cagini, C., et al.: Improvement of retinal OCT angiograms by sampling Kantorovich algorithm in the assessment of retinal choroidal perfusion. Appl. Math. Comput. **427**, 127152 (2022)
15. Carroll, J., et al.: Variability of foveal avascular zone metrics derived from optical coherence tomography angiography images. Transl. Vis. Sci. Technol. **5**(7), 20 (2018)
16. Çetin, N., Acu, A.M.: Approximation by α–Bernstein–Schurer–Stancu Operators. J. Math. Inequalities **15**(2), 845–860 (2021)
17. Chen, H., Cheung, C.Y., Fang, D., Lin, A.: Improved automated foveal avascular zone measurement in Cirrus optical coherence tomography angiography using the level sets macro. Transl. Vis. Sci. Technol. **12**(9), 20 (2020)
18. Chua, J., et al.: Optical coherence tomography angiography in diabetes and diabetic retinopathy. J. Clin. Med. **9**(6), 1723 (2020)
19. Costarelli, D., Sambucini, A.R.: Approximation results in Orlicz spaces for sequences of Kantorovich max-product neural network operators. RM **73**(1), 15 (2018)
20. Costarelli, D., Seracini, M., Travaglini, A., Vinti, G.: Alzheimer biomarkers esteem by sampling Kantorovich algorithm. Math. Methods Appl. Sci. **46**(12), 13506–13520 (2023)
21. Costarelli, D., Seracini, M., Vinti, G.: A segmentation procedure of the pervious area of the aorta artery from CT images without contrast medium. Math. Methods Appl. Sci. **43**, 114–133 (2020)

22. Costarelli, D., Seracini, M., Vinti, G.: A comparison between the sampling Kantorovich algorithm for digital image processing with some interpolation and quasi-interpolation methods. Appl. Math. Comput. **374**(2), 1–18 (2020)
23. Costarelli, D., Vinti, G.: Approximation by multivariate generalized sampling Kantorovich operators in the setting of Orlicz spaces. Bollettino dell'unione Matematica Italiana **4**(3), 445–468 (2011)
24. Costarelli, D., Vinti, G.: Approximation properties of the sampling Kantorovich operators: regularization, saturation, inverse results and Favard classes in L^p-spaces. J. Fourier Anal. Appl. **28**(3), 49 (2022)
25. Freeman, H.: On the encoding of arbitrary geometric configurations. IRE Trans. Electron. Comput. **10**(2), 260–268 (1961)
26. Freiberg, F.J., Pfau, M., Wons, J., Wirth, M.A., Becker, M.D., Michels, S.: Optical coherence tomography angiography of the foveal avascular zone in diabetic retinopathy. Graefes Arch. Clin. Exp. Ophthalmol. **254**, 1051–1058 (2016)
27. Gonzalez, R.C., Woods, R.E.: Digital Image Processing. Pearson Prentice Hall (2008)
28. Krawitz, B.D., et al.: Acircularity index and axis ratio of the foveal avascular zone in diabetic eyes and healthy controls measured by optical coherence tomography angiography. Vision. Res. **139**, 177–186 (2017)
29. Lo, A.C.Y., Wang, W.: Diabetic retinopathy: pathophysiology and treatments. Int. J. Mol. Sci. **19**(6), 1816 (2018)
30. Kumar, S., Mittal, H., Modwel, G., Pal, R., Pandey, A.C., Saraswat, M.: A comprehensive survey of image segmentation: clustering methods, performance parameters, and benchmark datasets. Multimedia Tools Appl. **81**, 35001–35026 (2022)
31. Oliverio, G.W., Ceravolo, I., Bhatti, A., Trombetta, C.J.: Foveal avascular zone analysis by optical coherence tomography angiography in patients with type 1 and 2 diabetes and without clinical signs of diabetic retinopathy. Int. Ophthalmol. **41**, 649–658 (2021)
32. Otsu, N.: A threshold selection method from Gray-level histograms. IEEE Trans. Syst. Man Cybern. Syst. **9**(1), 62–66 (1979)
33. Phansalkar, N., More, S., Sabale, A., Joshi, M.: Adaptive local thresholding for detection of nuclei in diversity stained cytology images. In: International Conference on Communications and Signal Processing, pp. 218–220 (2011)
34. Provis, J.M.: Development of the primate retinal vasculature. Prog. Retin. Eye Res. **20**(6), 799–821 (2001)
35. Sander, B., Larsen, M., Thrane, L., Hougaard, J.L., Jørgensen, T.M.: Enhanced optical coherence tomography imaging by multiple scan averaging. Br. J. Ophthalmol. **89**(2), 207–212 (2005)
36. Skarbez, K., Priestley, Y., Hoepf, M., Koevary, S.B.: Comprehensive review of the effects of diabetes on ocular health. Expert Rev. Ophthalmol. **5**(4), 557–577 (2010)
37. Spaide, R.F., Ledesma-Gil, G.: Novel method for image averaging of optical coherence tomography angiography images. Retina **40**(11), 2099–2105 (2020)
38. Thevenaz, P., Ruttimann, U.E., Unser, M.: A pyramid approach to subpixel registration based on intensity. IEEE Trans. Image Process. **7**(1), 27–41 (1998)
39. Travaglini, A., Vinti, G.: A mathematical model for the analysis of eye fundus images in healthy and diabetic patients. Lect. Notes Comput. Sci. **14108**, 558–576 (2023)
40. Travaglini, A., Vinti, G., Scalera, G.B., Scialpi, M.: A large scale analysis for testing a mathematical model for the study of vascular pathologies. Mathematics **11**(8), 1–19 (2023)

41. Vinti, G., Zampogni, L.: Approximation results for a general class of Kantorovich type operators. Adv. Nonlinear Stud. **14**(4), 991–1011 (2014)
42. Wang, Z., Bovik, A.C., Sheikh, H.R., Simoncelli, E.P.: Image quality assessment: from error visibility to structural similarity. IEEE Trans. Image Process. **13**(4), 600–612 (2004)
43. ImageJ: level sets. https://imagej.net/plugins/level-sets
44. MathWorks: Pixel values and image statistics, MATLAB. https://it.mathworks.com/help/images/pixel-values-and-image-statistics.html?s_tid=CRUX_topnav